

See discussions, stats, and author profiles for this publication at: <https://www.researchgate.net/publication/277252828>

# Multiple structural transformations coupled with switchable magnetic and dielectric responses in an amphidynamic crystal of 4'-tert-butylbenzylpyridinium bis(maleonitriledithiola...

ARTICLE · MAY 2015

DOI: 10.1039/C5TC00676G

---

READS

30

7 AUTHORS, INCLUDING:



[Xiao-Ming Ren](#)

Nanjing University of Technology

325 PUBLICATIONS 3,379 CITATIONS

SEE PROFILE



[Wei-Hua Ning](#)

Nanjing Tech University

19 PUBLICATIONS 26 CITATIONS

SEE PROFILE



[Katsuya Inoue](#)

Hiroshima University

1,242 PUBLICATIONS 25,356 CITATIONS

SEE PROFILE

## PAPER



Cite this: *J. Mater. Chem. C*, 2015, **3**, 7906

# Multiple structural transformations coupled with switchable magnetic and dielectric responses in an amphidynamic crystal of 4'-*tert*-butylbenzylpyridinium bis(maleonitriledithiolate)nickelate<sup>†</sup>

Wei-Hua Ning,<sup>ab</sup> Lu Zhai,<sup>ab</sup> Jian-Lan Liu,<sup>ab</sup> Xiao-Ming Ren,<sup>\*abc</sup> Katsuya Ichihashi,<sup>d</sup> Sadafumi Nishihara<sup>\*d</sup> and Katsuya Inoue<sup>d</sup>

Multifunctional materials that display different physical properties in a single phase can be utilized in multifunctional devices that are capable of performing more than one task simultaneously. In this study, we synthesized a novel multiple phase transition charge transfer salt [4'-*t*Bu-BzPy][Ni(mnt)<sub>2</sub>] (4'-*t*Bu-BzPy<sup>+</sup> = 4'-*tert*-butylbenzyl-pyridinium, mnt<sup>2-</sup> = maleonitriledithiolate) by incorporating a *tert*-butyl group to control the rotational dynamics in the crystal and to pre-program the amphidynamic [Ni(mnt)<sub>2</sub>]<sup>-</sup> magnetic lattice. This salt experienced a two-step structural transformation to give three separate high, immediate and low temperature phases. Interestingly, two structural transformations were coupled to both hysteretic magnetic phase transitions at 187/192 K and 94/96 K, and to dielectric anomalies. These results will assist the design and preparation of novel multiple phase-transition materials harboring technologically important magnetic and dielectric properties.

Received 10th March 2015,  
Accepted 26th May 2015

DOI: 10.1039/c5tc00676g

www.rsc.org/MaterialsC

## Introduction

Multifunctional materials that exhibit different physical properties in a single phase have potential for use in multifunctional devices.<sup>1–9</sup> Ferromagnetic semiconductors are a typical multifunctional material that combines the capabilities of semiconductor quantum structures and ferromagnetic multilayers for simultaneous electrical, magnetic or optical responses.<sup>10,11</sup> Because there exists a large *sp*-*d* exchange interaction between the band electrons and the magnetic transition metal ions, a magnetically tunable band gap<sup>12</sup> and control of magnetism by means of electric fields<sup>13,14</sup> are simultaneously achievable in ferromagnetic semiconductors. Multiferroic materials are another example, and the coexistence

of magnetism and ferroelectricity is even more desirable for constructing multifunctional devices.<sup>15–17</sup>

In general, electrical, magnetic or optical responses tend to change abruptly in the vicinity of phase transitions, and phase-transition materials possessing this property may have applications in data storage, signal processing and switchable devices and have thus attracted considerable attention in the field of molecular-based materials.<sup>5,18–22</sup> Although crystal engineering has progressed remarkably over the past three decades in terms of the self-assembly of desirable functional materials,<sup>23–25</sup> challenges regarding the synthesis of multiple phase-transition materials still remain. Notably, amphidynamic crystals offer a promising platform for the development of bulk multifunctional materials that are suitable for use in artificial molecular machines.<sup>26,27</sup> Amphidynamic crystals are a type of condensed-phase matter that possess anisotropic molecular order and controllable dynamics.<sup>26,27</sup> Volume-conserving motion (dynamic disorder) occurs in these crystals and disorder-to-order structural transformations are generally associated with this phenomena.

Disorder-to-order structural transformations are widely believed to be coupled to dielectric anomalies<sup>28–32</sup> and in some cases, to paraelectric-to-ferroelectric transitions.<sup>33–38</sup> We noted that the nature of planar and electronically delocalized cores comprised of a central nickel ion surrounded by four sulfur atoms, and C=C units makes the nickel-bis-dithiolene complex anion an excellent candidate for constructing spin-Peierls-type magnetic phase transition materials.<sup>39–44</sup> Furthermore, the

<sup>a</sup> State Key Laboratory of Materials-Oriented Chemical Engineering and College of Science, Nanjing Tech University, Nanjing 210009, P. R. China.

E-mail: xmren@njtech.edu.cn; Fax: +86 25 58139481; Tel: +86 25 58139476

<sup>b</sup> College of Materials Science and Engineering, Nanjing Tech University, Nanjing 210009, P. R. China

<sup>c</sup> State Key Laboratory of Coordination Chemistry, Nanjing University, Nanjing 210093, P. R. China

<sup>d</sup> Department of Chemistry, Hiroshima University, 1-3-1, Kagamiyama, Higashi-hiroshima 739-8526, Japan. E-mail: snishi@hiroshima-u.ac.jp

<sup>†</sup> Electronic supplementary information (ESI) available: Crystallographic data of **1** at 89, 110, 170, 200, 250, 296, 350 and 400 K are available in CIF format. PRXD, IR spectra, temperature dependent dielectric permittivity for a single crystal of **1**, and packing diagrams at 89 K. CCDC 1039174, 1039175, 1039177, 1039178 and 1039180–1039183. For ESI and crystallographic data in CIF or other electronic format see DOI: 10.1039/c5tc00676g

magnetic phase transition present in these systems is probably triggered by a disorder-to-order structural transformation.<sup>45–47</sup> Therefore, it may be possible to construct electrical and magnetic multiple phase-transition materials by incorporating well-known high-symmetry substituents such as *tert*-butyl and trifluoromethyl groups with fast rotational dynamics into the nickel-bis-dithiolene magnetic lattice.<sup>26</sup>

Herein, we report the development of a charge-transfer-type multiple phase-transition material,  $[4'\text{-}t\text{Bu-BzPy}][\text{Ni}(\text{mnt})_2]$  ( $4'\text{-}t\text{Bu-BzPy}^+ = 4'\text{-tert-butyl-benzylpyridinium}$ ,  $\text{mnt}^{2-} = \text{maleonitriledithiolate}$ ). The *tert*-butyl group appears to display fast rotational dynamics and the material undergoes two-step structural transformations in the 1.99–400 K range that are coupled to both hysteretic magnetic phase transitions and dielectric anomalies.

## Experimental

### Chemicals and materials

The starting materials  $\text{Na}_2\text{mnt}$ ,<sup>48</sup>  $[4'\text{-}t\text{Bu-BzPy}]\text{Cl}$  and  $[4'\text{-}t\text{Bu-BzPy}]_2\text{[Ni}(\text{mnt})_2]$  were synthesized using procedures similar to those previously reported in the literature.<sup>39</sup>

**Preparation of  $[4'\text{-}t\text{Bu-BzPy}][\text{Ni}(\text{mnt})_2]$ .** A MeOH solution (10 cm<sup>3</sup>) of  $\text{I}_2$  (205 mg, 0.80 mmol) was slowly added to a MeCN solution (20 cm<sup>3</sup>) of  $[4'\text{-}t\text{Bu-BzPy}]_2\text{[Ni}(\text{mnt})_2]$  (790 mg, 1.0 mmol) and the mixture was allowed to stand overnight following stirring for 30 min. The microcrystalline product formed was filtered, washed with MeOH and dried in vacuum. Yield = ~75%. Anal. calc. for  $\text{C}_{24}\text{H}_{20}\text{N}_5\text{NiS}_4$ : C, 50.98; H, 3.57; N, 12.39%. Found: C, 51.09; H, 3.38; N, 12.47%.

Crystals of **1** that were suitable for single crystal X-ray diffraction were obtained by the slow evaporation of the saturated acetonitrile solution of the abovementioned microcrystalline sample at ambient temperature for 7–10 days.

### Physical measurements

Elemental analyses for C, H and N were performed with an Elementar Vario EL III analytical instrument. Powder X-ray diffraction (PXRD) data were collected on a Bruker D8 diffractometer with Cu K $\alpha$  radiation ( $\lambda = 1.5418 \text{ \AA}$ ). FT-IR spectra were recorded on an IF66V FT-IR (4000–500 cm<sup>−1</sup>) spectrophotometer with KBr pellets. Differential scanning calorimetry (DSC) was carried out on a Pyris 1 power-compensation differential scanning calorimeter in the range of 103–303 K. Owing to the limitations of the instrument, it was not possible to measure  $T_{\text{C}}$  in the low-temperature phase (below 90 K). The warming/cooling rate was 10 K min<sup>−1</sup> during thermal cycling, and the heat capacity ( $C_{\text{p}}$ ) was measured following a relaxation method using a Quantum Design PPMS system over a temperature range of 69–121 K for the cooling process. We attached a crystal with dimensions of  $1.0 \times 1.0 \times 0.3 \text{ mm}^3$  and a mass of 0.43 mg to the sample platform using a small amount of grease, but unfortunately the crystal cracked during the measurement and we failed to obtain a full useable dataset. We subsequently formed a pellet from a powdered sample (0.41 mg) at 8 MPa

and performed a  $C_{\text{p}}$  measurement. Magnetic susceptibilities were measured on a Quantum Design MPMS-5 superconducting quantum interference device (SQUID) magnetometer over a temperature range of 1.99–400 K. Temperature-dependent dielectric permittivity,  $\epsilon'$ , was measured using an Agilent E4980A Precision LCR meter between 5 and 300 K. The pellet was made from a powdered sample of **1** for this measurement and the AC frequencies spanned from  $10^4$  to  $10^6 \text{ Hz}$ .

Solid state  $^1\text{H}$  NMR measurements were carried out on powdered crystals of **1** using a Bruker 300M AVANCE-II with a 90 degree pulse of 3  $\mu\text{s}$  and a recycle delay of 5 s. T1 was measured by a saturation recovery pulse sequence and measurements were made between 160 and 250 K.

### X-ray crystallography

Selected crystals of **1** were centered on an Oxford Diffraction Xcalibur diffractometer equipped with a Sapphire 3 CCD detector and a graphite monochromator using Cu K $\alpha$  ( $\lambda = 1.54178 \text{ \AA}$ ) or Mo K $\alpha$  ( $\lambda = 0.71073 \text{ \AA}$ ) radiation. Measurements were performed on **1** at 400, 350, 296, 250 and 200 K in the high-temperature (HT) phase, 170 and 110 K in the intermediate (IT) phase, and 89 K in the low-temperature (LT) cooling mode phase.

Data collection, unit cell refinement and data processing were carried out with the program CrysAlis.<sup>49</sup> Structures were solved by direct methods and refined using a full-matrix least-squares procedure on  $F^2$  using the SHELXL-97 program.<sup>50</sup> Non-hydrogen atoms were anisotropically refined and hydrogen atoms were placed at calculated positions and refined as riding on parent atoms. Disorder models were used for the *tert*-butyl (*t*Bu) group during the structural refinement of **1** in the HT phase at 400, 350, 296, 250 and 200 K. The *t*Bu group was assumed to have two sets of possible sites (although in reality there are probably more than two) and the occupation factor of each site was refined at each selected temperature.

Crystallographic details from the data collection and structural refinement are summarized in Tables 1 and 2. The bond lengths and angles of the anion moieties comparable to values previously reported for  $[\text{Ni}(\text{mnt})_2]^-$  crystals<sup>39</sup> at various temperatures in the HT, IT and LT phases fell within the expected value ranges and are summarized in Tables S1 and S2 (ESI†).

## Results and discussion

### Magnetic properties

The temperature dependence of the magnetic susceptibility of **1**, measured in both cooling and heating modes over a temperature range of 1.99–400 K, are shown in Fig. 1, where  $\chi_{\text{m}}$  represents the molar magnetic susceptibility of one  $[\text{Ni}(\text{mnt})_2]^-$  per formula unit of  $[4'\text{-}t\text{Bu-BzPy}][\text{Ni}(\text{mnt})_2]$ . Two-step hysteretic magnetic phase transitions (Fig. 1a and b) were observed with  $T_{\text{C1}\downarrow} \approx 187 \text{ K}$ ,  $T_{\text{C1}\uparrow} \approx 192 \text{ K}$  and  $\Delta T_1 \approx 5 \text{ K}$  for the transition between IT and LT phases *versus*  $T_{\text{C2}\downarrow} \approx 94 \text{ K}$ ,  $T_{\text{C2}\uparrow} \approx 96 \text{ K}$  and  $\Delta T_2 \approx 2 \text{ K}$  for the transition between HT and IT phases.

On the basis of the structural analysis (discussed more fully in the next section), only one crystallographically independent

**Table 1** Crystal data and structural refinement of **1** in the HT phase at 200, 250, 296, 350 and 400 K

Temp. (K)	200 K	250 K	296 K	350 K	400 K
Wavelength (Å)	1.54178	1.54178	0.71073	1.54178	1.54178
Formula	C <sub>24</sub> H <sub>20</sub> N <sub>5</sub> NiS <sub>4</sub>	C <sub>24</sub> H <sub>20</sub> N <sub>5</sub> NiS <sub>4</sub>	C <sub>24</sub> H <sub>20</sub> N <sub>5</sub> NiS <sub>4</sub>	C <sub>24</sub> H <sub>20</sub> N <sub>5</sub> NiS <sub>4</sub>	C <sub>24</sub> H <sub>20</sub> N <sub>5</sub> NiS <sub>4</sub>
Formula weight	565.38	565.38	565.38	565.38	565.38
Space group	<i>P</i> $\bar{1}$	<i>P</i> $\bar{1}$	<i>P</i> $\bar{1}$	<i>P</i> $\bar{1}$	<i>P</i> $\bar{1}$
CCDC	1039178	1039180	1039181	1039182	1039183
Crystal system	Triclinic	Triclinic	Triclinic	Triclinic	Triclinic
<i>a</i> (Å)	9.1729(6)	9.2268(6)	9.2682(14)	9.3162(9)	9.3555(11)
<i>b</i> (Å)	11.8460(8)	11.9210(9)	11.9800(14)	12.0910(11)	12.1960(12)
<i>c</i> (Å)	13.1452(9)	13.1309(10)	13.0643(16)	13.0809(13)	13.0415(14)
$\alpha$ (°)	72.777(6)	72.801(7)	72.936(4)	73.081(8)	73.212(9)
$\beta$ (°)	80.246(6)	80.517(6)	80.962(4)	81.247(8)	81.693(9)
$\gamma$ (°)	72.508(6)	72.197(6)	71.930(3)	71.461(8)	71.004(10)
<i>V</i> (Å <sup>3</sup> )/ <i>Z</i>	1296.2(15)/2	1309.2(16)/2	1314.8(3)/2	1333.6(2)/2	1344.9(3)/2
Density (g cm <sup>-3</sup> )	1.449	1.434	1.428	1.408	1.396
Abs coeff. (mm <sup>-1</sup> )	4.270	4.228	1.078	4.151	4.116
<i>F</i> (000)	582	582	582	582	582
Data collect $\theta$ range	3.53–70.72	3.54–70.74	2.13–25.50	3.54–70.71	3.55–70.85
Index range	–11 ≤ <i>h</i> ≤ 11 –14 ≤ <i>k</i> ≤ 14 –16 ≤ <i>l</i> ≤ 15	–11 ≤ <i>h</i> ≤ 11 –14 ≤ <i>k</i> ≤ 14 –16 ≤ <i>l</i> ≤ 15	–11 ≤ <i>h</i> ≤ 11 –14 ≤ <i>k</i> ≤ 14 –15 ≤ <i>l</i> ≤ 15	–11 ≤ <i>h</i> ≤ 11 –14 ≤ <i>k</i> ≤ 14 –15 ≤ <i>l</i> ≤ 15	–11 ≤ <i>h</i> ≤ 11 –14 ≤ <i>k</i> ≤ 14 –15 ≤ <i>l</i> ≤ 15
<i>R</i> <sub>int</sub>	0.0296	0.0293	0.0445	0.0277	0.0329
Independent reflect./restraints/parameters	4883/0/341	4922/0/341	4896/0/335	5013/0/341	5054/0/343
Refinement method	Least squares refinement of <i>F</i> <sup>2</sup>				
Goodness-of-fit of <i>F</i> <sup>2</sup>	1.061	1.057	1.025	1.022	1.010
<i>R</i> <sub>1</sub> , <i>wR</i> <sub>2</sub> <sup>a</sup> [ <i>I</i> > 2σ( <i>I</i> )]	0.0570, 0.1464	0.0611, 0.1539	0.0471, 0.1101	0.0669, 0.1753	0.0745, 0.1887
<i>R</i> <sub>1</sub> , <i>wR</i> <sub>2</sub> <sup>a</sup> [all data]	0.0636, 0.1541	0.0701, 0.1664	0.0801, 0.1193	0.0881, 0.2009	0.1089, 0.2462
Residual (e Å <sup>-3</sup> )	0.506/–0.777	0.455/–0.808	0.232/–0.361	0.376/–0.685	0.339/–0.743

$$^a R_1 = \sum(|F_o| - |F_c|)/\sum|F_o|, wR_2 = [\sum w(|F_o|^2 - |F_c|^2)^2/\sum w(|F_o|^2)^2]^{1/2}.$$

**Table 2** Crystal data and structural refinement of **1** in the LT phase at 89 K and in the IT phase at 110 and 170 K

Temp. (K)	89 K	110 K	170 K
Wavelength (Å)	1.54178	1.54178	1.54178
Formula	C <sub>24</sub> H <sub>20</sub> N <sub>5</sub> NiS <sub>4</sub>	C <sub>24</sub> H <sub>20</sub> N <sub>5</sub> NiS <sub>4</sub>	C <sub>24</sub> H <sub>20</sub> N <sub>5</sub> NiS <sub>4</sub>
Formula weight	565.38	565.38	565.38
Space group	<i>P</i> $\bar{1}$	<i>P</i> $\bar{1}$	<i>P</i> $\bar{1}$
CCDC	1039174	1039175	1039177
Crystal system	Triclinic	Triclinic	Triclinic
<i>a</i> (Å)	12.5624(5)	12.5675(4)	12.5916(5)
<i>b</i> (Å)	24.0375(10)	24.0765(7)	24.3127(9)
<i>c</i> (Å)	26.6188(11)	26.6120(8)	26.5376(9)
$\alpha$ (°)	74.498(4)	74.500(3)	74.657(3)
$\beta$ (°)	79.058(4)	78.987(3)	79.235(3)
$\gamma$ (°)	83.756(3)	83.749(3)	84.044(3)
<i>V</i> (Å <sup>3</sup> )/ <i>Z</i>	7590.5(5), 12	7602.3(4), 12	7684.0(5), 12
Density (g cm <sup>-3</sup> )	1.484	1.482	1.466
Abs coeff. (mm <sup>-1</sup> )	4.375	4.369	4.322
<i>F</i> (000)	3492	3492	3492
Data collect $\theta$ range	2.90–71.78	3.54–70.78	3.54–70.91
Index range	–11 ≤ <i>h</i> ≤ 11 –11 ≤ <i>k</i> ≤ 11 –11 ≤ <i>l</i> ≤ 11	–14 ≤ <i>h</i> ≤ 15 –29 ≤ <i>k</i> ≤ 28 –32 ≤ <i>l</i> ≤ 31	–14 ≤ <i>h</i> ≤ 15 –29 ≤ <i>k</i> ≤ 28 –32 ≤ <i>l</i> ≤ 31
<i>R</i> <sub>int</sub>	0.0685	0.0438	0.0455
Independent reflect./restraints/parameters	28 939/0/1855	28 645/0/1855	28 948/0/1837
Refinement method	Least squares refinement of <i>F</i> <sup>2</sup>		
Goodness-of-fit of <i>F</i> <sup>2</sup>	0.874	1.031	0.883
<i>R</i> <sub>1</sub> , <i>wR</i> <sub>2</sub> <sup>a</sup> [ <i>I</i> > 2σ( <i>I</i> )]	0.0630, 0.1710	0.0551, 0.1429	0.0615, 0.1617
<i>R</i> <sub>1</sub> , <i>wR</i> <sub>2</sub> <sup>a</sup> [all data]	0.1132, 0.2238	0.0699, 0.1562	0.0861, 0.1913
Residual (e Å <sup>-3</sup> )	1.316/–0.711	0.777/–0.994	0.773/–0.928

$$^a R_1 = \sum(|F_o| - |F_c|)/\sum|F_o|, wR_2 = [\sum w(|F_o|^2 - |F_c|^2)^2/\sum w(|F_o|^2)^2]^{1/2}.$$

[Ni(mnt)<sub>2</sub>]<sub>2</sub><sup>2-</sup> dimer was present in the HT phase, whereas there were three crystallographically different dimers in both the IT and LT phases. It was assumed that the magnetic exchange

constants within the three different [Ni(mnt)<sub>2</sub>]<sub>2</sub><sup>2-</sup> dimers in both the IT and LT phases were the same, and that the magnetic coupling differences between [Ni(mnt)<sub>2</sub>]<sub>2</sub><sup>2-</sup> dimers were negligible

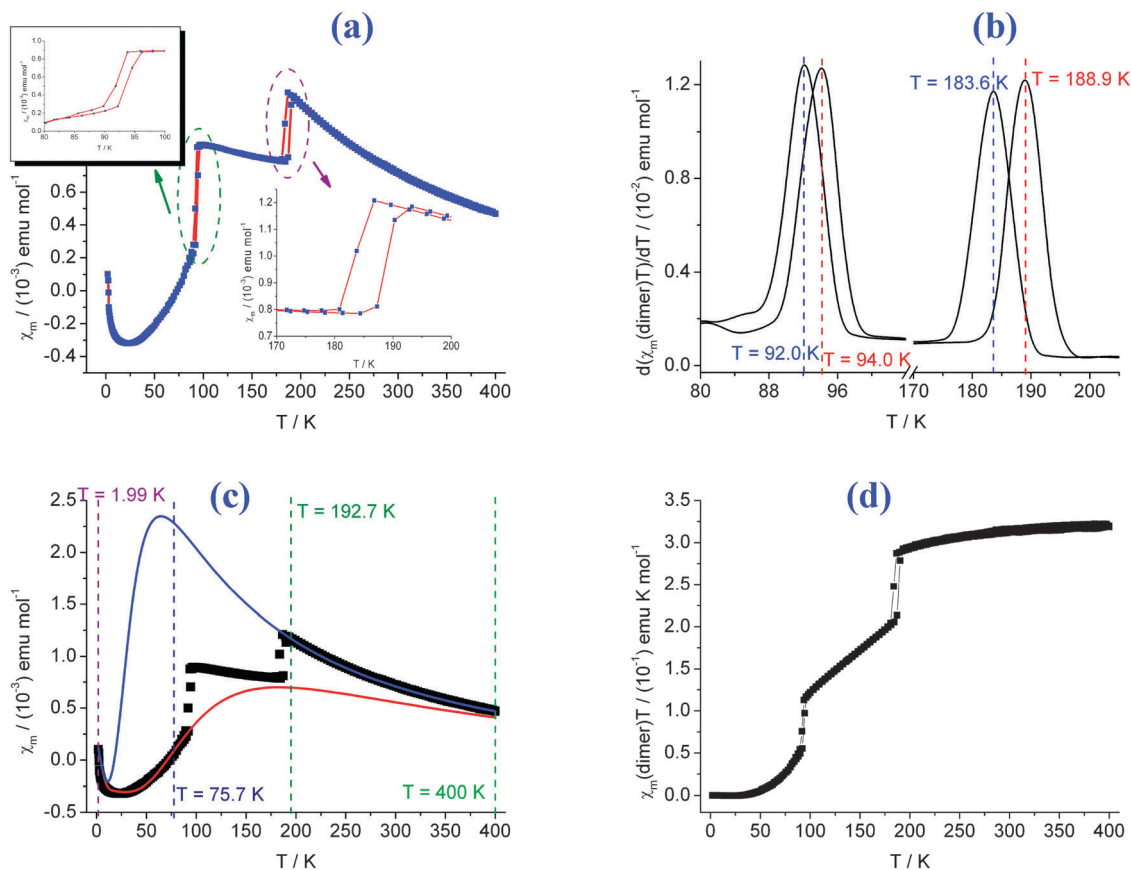


**Fig. 1** Plots of (a)  $\chi_m$  vs.  $T$  (insets = thermal hysteresis loops), (b)  $d(\chi_m T)/dT$ , (c) experimental magnetic susceptibility in the cooling mode (solid squares). Theoretically reproduced plots were constructed using fitting parameters from HT (blue line) and LT (red line) phases, respectively. (d) Plots of  $\chi_m(\text{chain})T$  vs.  $T$ , where  $\chi_m(\text{chain})$  is the magnetic susceptibility contribution from spin chains.

compared with those within a dimer. Magnetic susceptibility data were analyzed using a spin dimer model that considers it as a function of temperature and is given by eqn (1) for a spin dimer with two  $S = 1/2$  spins, as deduced from the spin Hamiltonian

$$\hat{H} = -2J\hat{S}_1 \cdot \hat{S}_2$$

$$\chi_{\text{dimer}} = \frac{Ng^2\beta^2}{k_B T} \left[ 3 + \exp\left(-\frac{2J}{k_B T}\right) \right]^{-1} \quad (1)$$

where  $g$  is the Landé factor,  $J$  represents the magnetic exchange constant within the spin dimer, and all other symbols have the usual meanings. To further consider paramagnetic impurities and temperature-independent paramagnetism, experimental molar magnetic susceptibility can be described by eqn (2)

$$\chi_m = (1 - \rho)\chi_{\text{dimer}} + \rho \frac{C}{T - \theta} + \chi_0 \quad (2)$$

where  $\rho$  represents the molar fraction of uncoupled magnetic impurity in the crystal. Paramagnetic impurity originates from lattice defects and follows the Curie-Weiss law,  $C/(T - \theta)$ , whereas temperature-independent paramagnetism ( $\chi_0$ ) arises from both atom core diamagnetism and possibly also from van Vleck paramagnetism, which is associated with the coupling of the ground and excited states through the magnetic field.<sup>51</sup>

A best fit of the magnetic susceptibility data was performed over a range of 1.99–75.7 K to obtain the parameters  $J/k_B = -147(1)$  K,  $\rho = 1.43(1) \times 10^{-3}$  emu K mol<sup>-1</sup>,  $\theta = 0.8(1)$  K and  $\chi_0 = -3.3(7) \times 10^{-4}$  emu mol<sup>-1</sup>, with  $g = 2.0$  fixed in the LT phase. The theoretical plot of  $\chi_m$  vs.  $T$  was reproduced in the range of 1.99–400 K using the fitted parameters from the LT phase (Fig. 1c).

The amount of magnetic impurity and the temperature-independent magnetic susceptibility in both IT and HT phases were estimated to be the same as those in the LT phase, and a best fit of the magnetic susceptibility data was carried out over the range of 192.7–400 K to yield the parameters  $J/k_B = -51(1)$  K with  $g = 1.91(0)$  in the HT phase. The theoretically reproduced plot of  $\chi_m$  vs.  $T$  (Fig. 1c) was constructed using the fitted parameters  $J/k_B$  and  $g$  from the HT phase and the magnetic impurity and  $\chi_0$  terms from the LT phase. Notably, this approach was unable to give reasonable parameters through fitting variable-temperature magnetic susceptibility data in the IT phase using eqn (2). Fitting of magnetic susceptibility data in both HT and LT phases disclosed the existence of an antiferromagnetic (AFM) coupling interaction within the  $[\text{Ni}(\text{mnt})_2]^{2-}$  dimer in **1**, which was strengthened in going from the HT to the LT phase due to a decrease in the plane-to-plane distance between the mean-molecule-planes of  $[\text{Ni}(\text{mnt})_2]^-$  anions. This is understandable given that the AFM coupling constant  $J_{\text{AF}} \propto -(2t)^2/U_{\text{eff}}$ , where



$U_{\text{eff}}$  is the effective on-site repulsion and is almost constant for a defined magnetic solid, and  $t$  is the transfer integral between the spin sites, which is proportional to the overlapping integral of the interaction magnetic orbitals.<sup>52</sup> The overlap of magnetic orbitals increased between HT and LT phases, and the plane-to-plane distance between  $[\text{Ni}(\text{mnt})_2]^-$  anions within a dimer therefore decreased.

The magnetic susceptibility  $\chi_{\text{m}}(\text{dimer})$ , contributed from the dimers, was obtained by subtracting two terms from  $C/(T - \theta)$  along with  $\chi_0$  from the experimental magnetic susceptibility, and the corresponding  $\chi_{\text{m}}(\text{dimer})T$  values were plotted against  $T$  (Fig. 1d). The  $\chi_{\text{m}}(\text{dimer})T$  value gradually decreased from  $0.320 \text{ emu mol}^{-1}$  at 400 K to  $0.291 \text{ emu mol}^{-1}$  at 196 K in the HT phase owing to weakly antiferromagnetic coupling within the dimer. This value reached zero upon cooling to *ca.* 25 K due to a strongly antiferromagnetic coupling within dimers in the LT phase.

### Crystal structures from the HT phase at 400, 350, 296, 250 and 200 K

Salt **1** crystallized in the triclinic space group  $P\bar{1}$  in the HT phase (Fig. 2) with an asymmetric unit comprised of a pair of  $[\text{Ni}(\text{mnt})_2]^-$  anions and one  $4'-t\text{Bu-BzPy}^+$  cation. The mean-molecule-plane of the  $[\text{Ni}(\text{mnt})_2]^-$  anion, defined through four coordinated S atoms, makes a dihedral angle of  $13.7^\circ$  with the phenyl ring of the cation. In the  $\Lambda$ -shaped  $4'-t\text{Bu-BzPy}^+$  cation, the disordered *t*Bu group was assumed to have two possible sites, and the occupation factor of each site was refined to be 0.66793/0.33207 in the HT phase (at 200 K). Cation bond lengths and angles fell within the expected ranges, and the dihedral angle of  $71.5^\circ$  between the phenyl and pyridyl rings was typical, as were the  $83.9^\circ$  and  $89.3^\circ$  angles between the reference plane N5–C14–C15 and the phenyl ring or pyridyl ring, respectively.

As shown in Fig. 3a and b, the anions and cations are aligned into mixed stacks, with alternating anionic (AA) and cationic (CC) dimers arranged in a ...AACCAACC... fashion along the crystallographic  $a + b$  direction. The mixed stacks form a molecular layer parallel to the crystallographic (1–10) plane. Within a cation dimer (Fig. 3c), two  $4'-t\text{Bu-BzPy}^+$  cations, which are related to each other *via* an inversion center, are

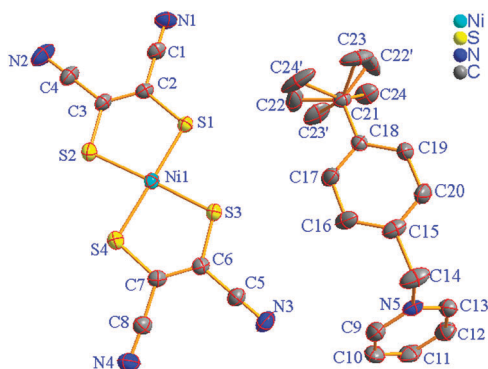


Fig. 2 ORTEP representation of **1** in the HT phase at 200 K. Non-hydrogen atom labelling is shown, and thermal ellipsoids are drawn at the 20% probability level. The two possible sites of the disordered *t*Bu group are visible.

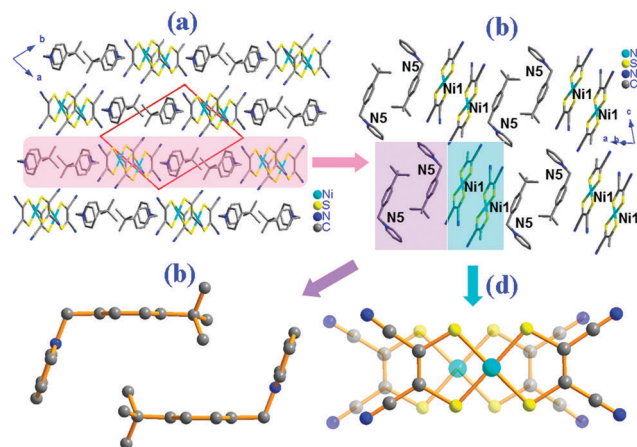


Fig. 3 (a) Packing of **1** at 200 K viewed along the  $c$ -axis. (b) The monolayer parallel to the (1–10) plane showing the alternating stacks of dimeric anions and dimeric cations along the  $a + b$  direction. (c) Cationic dimer displaying the chair-type alignment. (d) Anionic dimer in the longitudinal offset mode.

arranged in a chair-type alignment, where two phenyl rings are in an anti-parallel arrangement with a longer centroid-to-centroid separation ( $5.804 \text{ \AA}$ ) owing to the steric hindrance between the *t*Bu groups and the neighboring pyridyl/phenyl rings. Within each anion dimer, two  $[\text{Ni}(\text{mnt})_2]^-$  anions are stacked in the longitudinal offset mode, resulting in slightly longer interatomic separation with a  $d_{\text{plane-to-plane}} = 3.617 \text{ \AA}$ ,  $d_{\text{Ni}(1) \cdots \text{Ni}(1)\#1} = 4.100 \text{ \AA}$ ,  $d_{\text{S}(4) \cdots \text{S}(3)\#1} = 3.846 \text{ \AA}$ ,  $d_{\text{S}(1) \cdots \text{S}(4)\#1} = 4.057 \text{ \AA}$ ,  $d_{\text{S}(2) \cdots \text{S}(3)\#1} = 4.053 \text{ \AA}$ , where the symmetric code  $\#1 = 1 - x, -y, 1 - z$  (Fig. 3d).

The crystal structures of **1** at 400, 350, 250 and 296 K were essentially identical to that at 200 K, and the corresponding data are shown in the ESI.†

### Crystal structures from the IT phase at 170 and 110 K and the LT phase at 89 K

Crystal structures from the IT phase at 170 and 110 K were highly similar to each other, and the space group ( $P\bar{1}$ ) was the same as the HT phase. However, the asymmetric unit switched from containing one anion–cation pair in the HT phase to six anion–cation pairs in the IT phase (Fig. 4a), indicating a loss of translational symmetry. Compared with the structure from the HT phase, the unit cell approximately doubled in length along the  $c$ -axis and almost tripled along the  $b$ -axis, while the  $a$ -axis was only slightly extended (the  $a$ - and  $b$ -axes of the IT phase structure correspond roughly to the  $b$ - and  $a$ -axes of the HT phase structure). The conformations of six nonequivalent cations are clearly distinct from those in the HT phase, as reflected by the typical dihedral angles between the phenyl and pyridyl rings and between the phenyl/pyridyl ring and the reference plane (Table 2). In addition, the methyl groups are ordered in the IT phase with the exception of C95 and C96, which have an ADP max/min ratio of 3.5 and 4.8 at 170 K, respectively, indicating dynamic disorder up to 170 K. However, upon further cooling to 110 K in the IT phase, all *t*Bu groups in the cations became ordered.

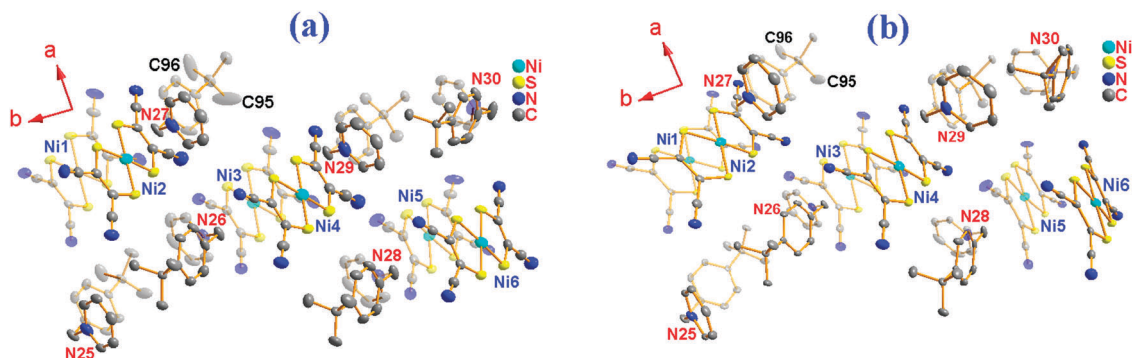


Fig. 4 ORTEP representation of **1** shows thermal ellipsoids drawn at the 20% probability level in the IT phase, where atoms are labelled in the usual manner and H atoms are omitted for clarity at: (a) 170 K and (b) 110 K.

The packing of **1** in the IT phase was very similar to that in the HT phase with molecular layers of anions and cations along the *a*-axis and mixed stacks arranged in the ...AACCAACC... fashion along the *b*-*c* direction within a monolayer (Fig. 5).

Only one type of anionic dimer and one type of cationic dimer are present in the HT phase (Fig. 3) and the broken translational symmetry gives rise to three different anionic dimers (Ni1Ni2, Ni3Ni4 and Ni5Ni6) as well as three different cationic dimers (N25N26, N27N28 and N29N30) in the IT phase (Fig. 5b).

Upon further cooling from 110 to 89 K, an isostructural phase transition occurred at *ca.* 94 K. The space group and asymmetric unit of the LT phase structure are the same as that of the IT phase; therefore, an isostructural phase transition (IPT) occurred between the IT and LT phases. The molecular packing of **1** was highly similar in the IT and LT phases (Fig. 5 and Fig. S1, ESI†). To compare structural changes in the three phases, we examined the variation in typical intermolecular distances, inter-planar distances and dihedral angles, which are summarized in Table S3 (ESI†). Alterations in unit cell parameters were also assessed. A plot of distances and dihedral angles (Fig. 6) showed that (1) as temperature decreases, the Ni...Ni and plane-to-plane distances between anions within an anion dimer, as well as the centroid-to-centroid distance between the phenyl rings within a cation dimer, linearly and gradually decrease in the HT phase. However, these typical

distances change abruptly following the symmetry-breaking phase transition from the HT to the IT phase. In addition, the dihedral angle between the phenyl rings within a cation dimer is also increased sharply below the temperature of the symmetry-breaking phase transition. (2) Between the IT and LT phases, the Ni...Ni and plane-to-plane distance between anions within an anion dimer showed little change, whereas the centroid-to-centroid distances between the phenyl rings within the cation dimers, which included N25/26 and N27/28, displayed considerable variation.

The temperature dependence of the cell parameters in the crystal structure of **1** revealed significant changes in going from the HT to the IT phase, but with minimal variation between the IT and LT phases (Fig. 7a and b). This further confirmed the occurrence of a symmetry-breaking phase transition between the HT to IT phases and the much stronger structural similarity between the IT and LT phases.

### Thermal analysis

Dynamic scanning calorimetry (DSC) of **1** across the 160–220 K range and a heating-cooling cycle revealed a pair of intensely endothermic and exothermic peaks around the transition temperature between the HT and IT phases, with an onset temperature  $T_{\uparrow} \approx 189.2$  K and  $T_{\downarrow} \approx 187.7$  K, respectively (Fig. 8a). The  $T_{\uparrow}$  and  $T_{\downarrow}$  temperatures were close to the  $T_C$  value

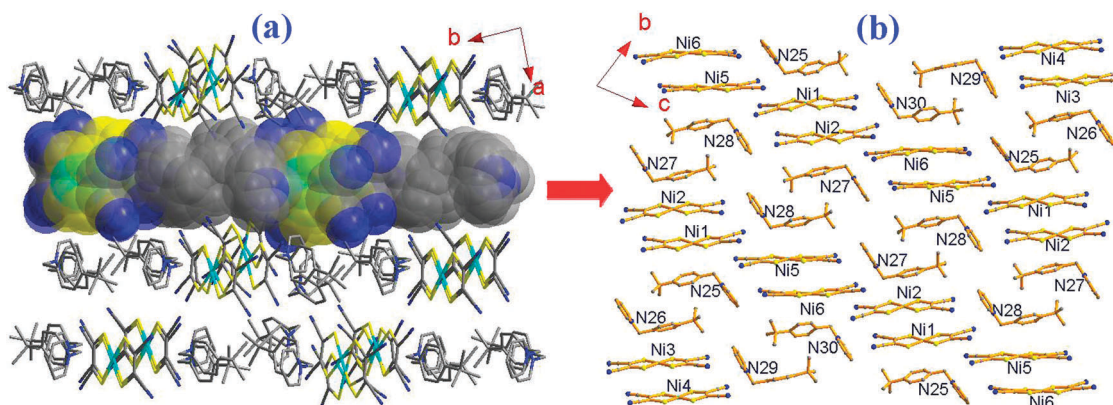


Fig. 5 (a) Packing of **1** viewed along the *c*-axis. (b) A single monolayer of **1** at 170 K in the IT phase.

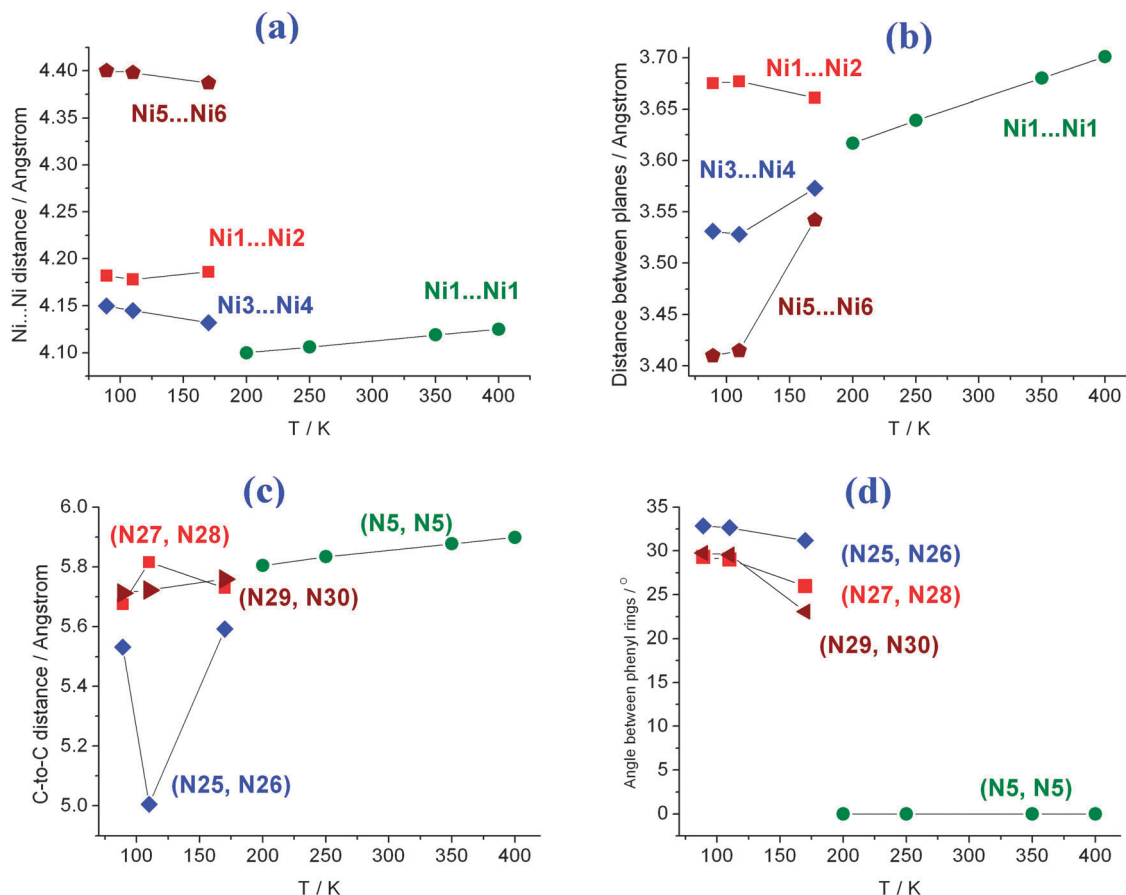


Fig. 6 Temperature dependent (a) Ni...Ni and (b) plane-to-plane distance within an anion dimer, and (c) centroid-to-centroid distance and (d) dihedral angle between the phenyl rings within a cation dimer.

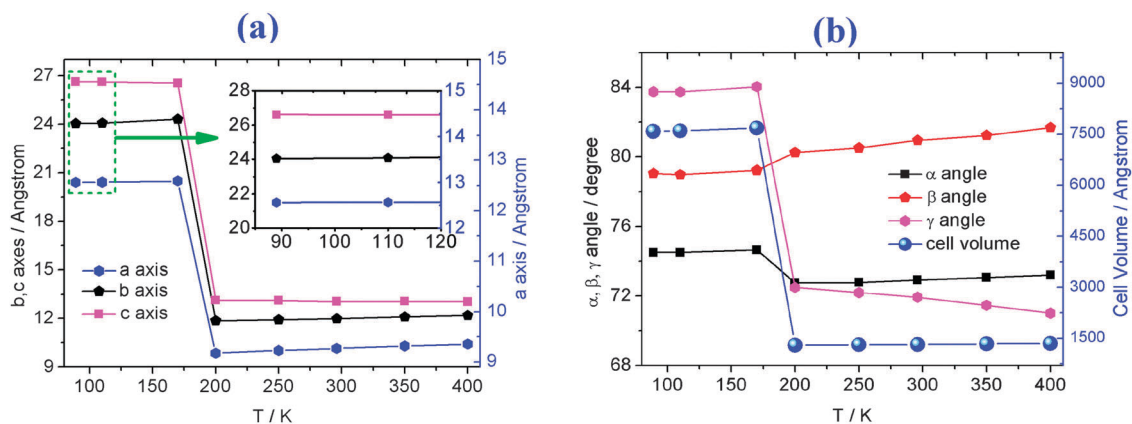


Fig. 7 Temperature dependence of the cell parameters in the crystal structure of **1**. (a) *a*, *b* and *c*-axes (b)  $\alpha$ ,  $\beta$ , and  $\gamma$  angles as well as cell volume *V* in the temperature range of 89–400 K.

obtained from the magnetic susceptibility measurement and the enthalpy difference ( $\Delta H$ ) between the HT and IT phases, calculated from the integrated peak area, was estimated to be 2172.3 J mol<sup>−1</sup> in heating mode (Fig. S2, ESI†). The corresponding entropy change ( $\Delta S$ ) was calculated to be 11.54 J K<sup>−1</sup> mol<sup>−1</sup> using equation  $\Delta S = \Delta H/T_C$  (where  $T_C$  is the critical temperature of the phase transition and was attributed the typical value of 189.2 K).

The  $\Delta S$  value includes contributions from the structure and the spin entropy differences between two phases (phases 1 and 2), and can be expressed in terms of statistical mechanics as follows:

$$\Delta S = R \ln \frac{\Omega_1}{\Omega_2} \quad (3)$$



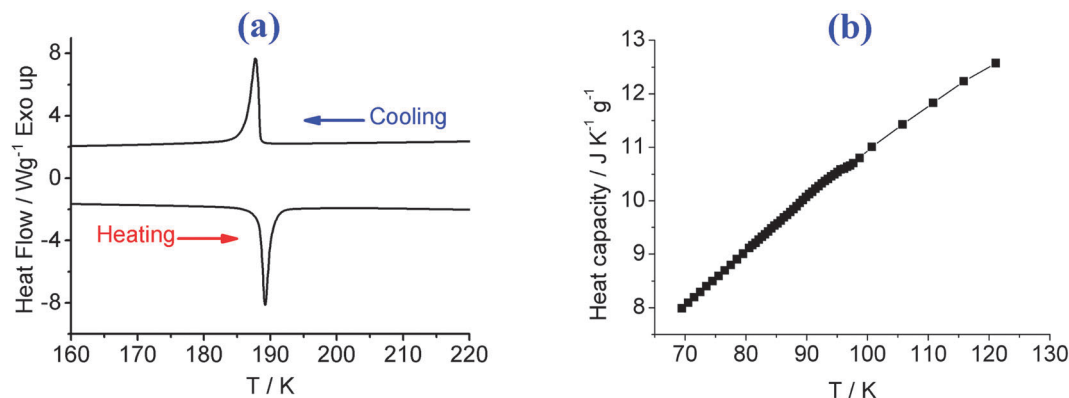


Fig. 8 Thermal analysis of **1**. (a) DSC plots with heating and cooling in the range of 160–220 K. (b)  $C_p$  plot measured upon cooling from 120 to 70 K.

where  $R$  ( $8.31 \text{ J K}^{-1} \text{ mol}^{-1}$ ) is the gas constant, and  $\Omega_i$  ( $i = 1$  and  $2$ ) represents the state numbers of phases 1 and 2, respectively. The values of  $\Omega_{\text{HT}}/\Omega_{\text{IT}}$  were estimated to be 3.98, indicating that the number of disordered sites of the *t*Bu group of the cation is probably greater than two (we initially assumed the *t*Bu group to have two possible sites in the process of refinement of the HT phase structure).

The heat capacity ( $C_p$ ) was calculated to investigate the thermal behavior of **1** in the IPT between the IT and LT phases. As shown in Fig. 8b, a broad and weak thermal anomaly peak occurred around 94 K in the plot of  $C_p$  versus  $T$ , implying a small entropy difference between the IT and LT phases. This result also supports a strong structural similarity between the IT and LT phases.

### Dielectric properties

The electric polarizability is a measure of the tendency of a material to allow an externally applied electric field to induce electric dipoles (separated positive and negative charges) in the material. Polarization  $P$  is related to the electric field  $E$  and the electric displacement  $D$  by

$$D = \epsilon_0 E + P \quad (4)$$

where  $P$  is related to  $E$  through  $\chi_e$ , the electric susceptibility of the dielectric  $P = \epsilon_0 \chi_e E$ , therefore

$$D = \epsilon_0 (1 + \chi_e) E = \epsilon_0 \epsilon_r E \quad (5)$$

$$P = \epsilon_0 (\epsilon_r - 1) E \quad (6)$$

where  $\epsilon_0$  and  $\epsilon_r$  represent the permittivity of the free space and the relative dielectric constant of a material. It is noted that  $P$  is also the density of the atomic electric dipole per unit volume

$$P = \sum p/V = Np \quad (7)$$

therefore

$$Np = \epsilon_0 (\epsilon_r - 1) E \quad (8)$$

where  $p$  is the dipole moment and  $N$  is the density of dipoles. As mentioned above, the  $\epsilon_r$  of a material is related to the dipole moment, which depends on the crystal structure. As a result, a structural phase transition probably leads to dielectric anomalies

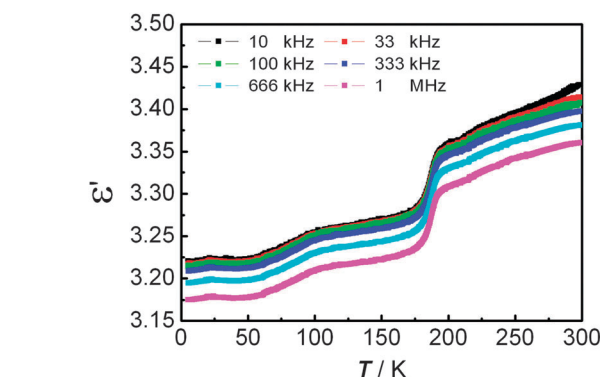


Fig. 9 Plots of dielectric permittivity  $\epsilon'$  against temperature  $T$  at selected AC frequencies. Measurement was carried during heating from 5 to 300 K.

if there are significant differences in the crystal structures between two different phases.<sup>29</sup>

The temperature dependent dielectric permittivity  $\epsilon'$  decreases rapidly at *ca.* 191 K then more gradually at *ca.* 96 K (Fig. 9). These values are close to the critical temperatures of the magnetic phase transition between the HT and IT phases, and between the IT and LT phases. This observation demonstrated that the dielectric anomaly is coupled to the corresponding magnetic and structural phase transitions. In addition, it was found that the phase transition, leading to the dielectric permittivity change  $\Delta\epsilon'$ , was larger between the HT and IT phases than between the IT and LT phases. This finding is in agreement with the crystal structure analyses and further confirmed the existence of significant structural differences between the HT and LT phases and the high structural similarity between the IT and LT phases.

### Solid-state $^1\text{H}$ NMR

Rotational dynamics in the solid state can be studied by  $^1\text{H}$  NMR spectroscopy, thus  $^1\text{H}$  solid state NMR spectra of **1** were measured over a temperature range of 160–250 K in the cooling process and over a chemical shift ( $\delta$ ) range of  $-3$  to 3 ppm. As demonstrated in Fig. 10a and b,  $^1\text{H}$  NMR signals arising from the H atoms of the *tert*-butyl group were shifted downfield upon cooling at temperatures above 170 K, but were

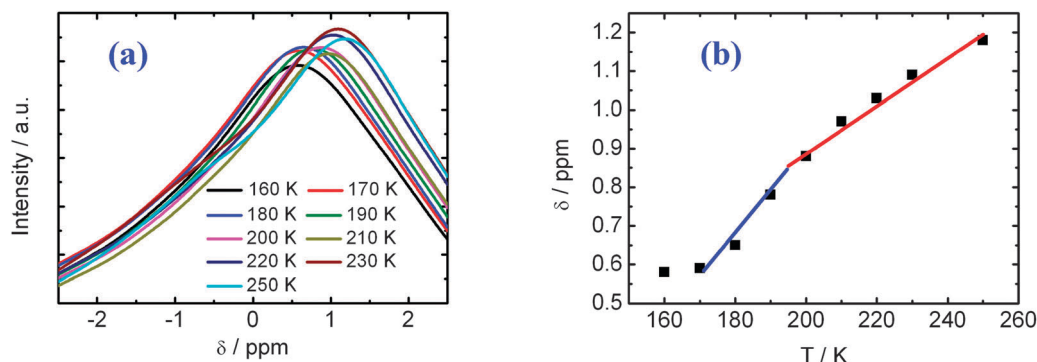


Fig. 10 (a)  $^1\text{H}$  NMR signals at selected temperatures (b) plot of  $^1\text{H}$  NMR signal peak position versus temperature.

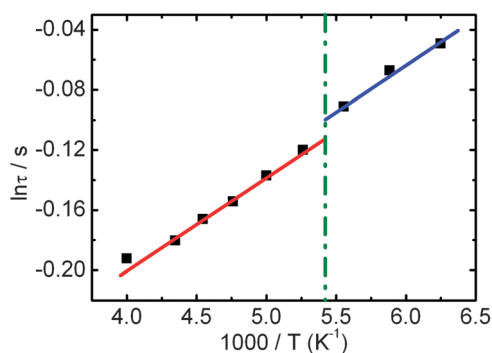


Fig. 11 Plot of  $\ln \tau$  vs.  $1000/T$ .

temperature-independent below 170 K owing to the freezing of rotational motion around the *tert*-butyl group  $C_3$  axis. From Fig. 10b, it is also clear that the slope of the plot of  $\delta$  vs.  $T$  is distinct and the crossover point of the two lines is close to the critical temperature of the phase transition between the HT and IT phases.

We performed variable-temperature solid-state  $^1\text{H}$  NMR spin-echo experiments to determine relaxation times at selected temperatures (Fig. 11). Assuming that relaxation is thermally activated, the relationship between relaxation time and temperature follows the Arrhenius law,

$$\ln \tau = \ln \tau_0 + \frac{E_a}{k_B T} \quad (9)$$

where  $E_a$  is the activation energy associated with the corresponding molecular motion and  $\tau_0$  is the pre-exponential factor. The best fits gave  $E_a = 711.3 \text{ J mol}^{-1}$  and pre-exponential factor  $\tau_0 = 0.566 \text{ s}$  for the IT phase, versus  $E_a = 548.1 \text{ J mol}^{-1}$  and pre-exponential factor  $\tau_0 = 0.631 \text{ s}$  for the HT phase.

## Conclusion

In summary, a multiple phase-transition material was prepared by incorporating well-characterized high-symmetry *tert*-butyl groups with fast rotational dynamics into crystals of a magnetically and electronically functional  $[\text{Ni}(\text{mnt})_2]^-$  lattice. A symmetry-breaking phase transition at *ca.* 192 K is associated with the loss of the

rotational freedom of *tert*-butyl groups upon transition from the HT to the IT phase. Furthermore, an isostructural phase transition occurred at *ca.* 96 K. These two structural phase transitions are coupled to the magnetic and dielectric phase transitions.

## Acknowledgements

Authors thank the Priority Academic Program Development of Jiangsu Higher Education Institutions, Special Research Found for the Doctoral Program of Higher Education and National Nature Science Foundation of China for financial support (grant no. 20123221110013, 91122011 and 21271103).

## Notes and references

- 1 M. E. Itkis, X. Chi, A. W. Cordes and R. C. Haddon, *Science*, 2002, **296**, 1443–1445.
- 2 O. Kahn and C. J. Martinez, *Science*, 1998, **279**, 44–48.
- 3 M. W. Gaultois, P. T. Barton, C. S. Birkel, L. M. Misch, E. E. Rodriguez, G. D. Stucky and R. Seshadri, *J. Phys.: Condens. Matter*, 2013, **25**, 186004.
- 4 B. C. Melot, A. Goldman, L. E. Darago, J. D. Furman, E. E. Rodriguez and R. Seshadri, *J. Phys.: Condens. Matter*, 2010, **22**, 506003.
- 5 P. P. Shi, Q. Ye, Q. Li, H. T. Wang, D. W. Fu, Y. Zhang and R. G. Xiong, *Chem. Mater.*, 2014, **26**, 6042–6049.
- 6 M. Wu, J. D. Burton, E. Y. Tsymbal, X. C. Zeng and P. Jena, *J. Am. Chem. Soc.*, 2012, **134**, 14423–14429.
- 7 E. Pardo, C. Train, H. Liu, L. M. Chamoreau, B. Dkhil, K. Boubekeur, F. Lloret, K. Nakatani, H. Tokoro, S.-i. Ohkoshi and M. Verdaguer, *Angew. Chem., Int. Ed.*, 2012, **51**, 8356–8360.
- 8 Y. Tokura and S. Seki, *Adv. Mater.*, 2010, **22**, 1554–1565.
- 9 E. Coronado, J. R. Galán-Mascarós, C. J. Gómez-García and V. Laukhin, *Nature*, 2000, **408**, 447–449.
- 10 T. Dietl, *Nat. Mater.*, 2010, **9**, 965–974.
- 11 J. K. Furdyna, *J. Appl. Phys.*, 1988, **64**, R29–R64.
- 12 Y. D. Kim, S. L. Cooper, M. V. Klein and B. T. Jonker, *Phys. Rev. B: Condens. Matter Mater. Phys.*, 1994, **49**, 1732–1742.
- 13 H. Ohno, D. Chiba, F. Matsukura, T. Omiya, E. Abe, T. Dietl, Y. Ohno and K. Ohtani, *Nature*, 2000, **408**, 944–946.

- 14 D. Chiba, M. Sawicki, Y. Nishitani, Y. Nakatani, F. Matsukura and H. Ohno, *Nature*, 2008, **455**, 515–518.
- 15 S. Cheong and M. Mostovoy, *Nat. Mater.*, 2007, **6**, 13–20.
- 16 R. Ramesh and N. A. Spaldin, *Nat. Mater.*, 2007, **6**, 21–29.
- 17 W. Eerenstein, N. D. Mathur and J. F. Scott, *Nature*, 2006, **442**, 759–765.
- 18 D. Lencer, M. Salinga and M. Wuttig, *Adv. Mater.*, 2011, **23**, 2030–2058.
- 19 M. Wuttig and N. Yamada, *Nat. Mater.*, 2007, **6**, 824–832.
- 20 H. K. Henisch, R. Roy and L. E. Cross, *Phase Transition*, Pergamon Press, New York, 1973.
- 21 D. Li, R. Clérac, O. Roubeau, E. Harté, C. Mathonière, R. Le Bris and S. M. Holmes, *J. Am. Chem. Soc.*, 2008, **130**, 252–258.
- 22 Y. Z. Zhang, P. Ferko, D. Siretanu, R. Ababei, N. P. Rath, M. J. Shaw, R. Clérac, C. Mathonière and S. M. Holmes, *J. Am. Chem. Soc.*, 2014, **136**, 16854–16864.
- 23 A. M. Guloy, Z. J. Tang, P. B. Miranda and V. I. Srdanov, *Adv. Mater.*, 2001, **13**, 833–835.
- 24 T. P. Radhakrishnan, *Acc. Chem. Res.*, 2008, **41**, 367–376.
- 25 G. R. Desiraju, *Angew. Chem., Int. Ed.*, 2007, **46**, 8342–8356.
- 26 M. A. Garcia-Garibay, *Proc. Natl. Acad. Sci. U. S. A.*, 2005, **102**, 10771–10776.
- 27 S. Cortnie and M. A. Garcia-Garibay, *Chem. Soc. Rev.*, 2012, **41**, 1892–1910.
- 28 W. Liao, G. Mei, H. Ye, Y. Mei and Y. Zhang, *Inorg. Chem.*, 2014, **53**, 8913–8918.
- 29 W. H. Ning, L. Zhai and X. M. Ren, *RSC Adv.*, 2014, **4**, 30993–30998.
- 30 A. Piecha, A. Gągor, A. Pietraszko and R. Jakubas, *J. Solid State Chem.*, 2010, **183**, 3058–3066.
- 31 H. B. Cui, K. Takahashi, Y. Okano, H. Kobayashi, Z. M. Wang and A. Kobayashi, *Angew. Chem., Int. Ed.*, 2005, **44**, 2–6.
- 32 R. Decressain, R. Jakubas, G. Bator, J. Zaleski, J. Lefebvre and J. Kusz, *J. Phys. Chem. Solids*, 1999, **58**, 1487–1498.
- 33 G. C. Xu, X. M. Ma, L. Zhang, Z. M. Wang and S. Gao, *J. Am. Chem. Soc.*, 2010, **132**, 9588–9590.
- 34 B. Kundys, A. Lappas, M. Viret, V. Kapustianyk, V. Rudyk, S. Semak, C. Simon and I. Bakaimi, *Phys. Rev. B: Condens. Matter Mater. Phys.*, 2010, **81**, 224434.
- 35 S. Horiuchi, R. Kumai, Y. Tokunaga and Y. Tokura, *J. Am. Chem. Soc.*, 2008, **130**, 13382–13391.
- 36 P. Czarnecki, W. Nawrocik, Z. Pająk and J. Wąsicki, *Phys. Rev. B: Condens. Matter Mater. Phys.*, 1994, **49**, 1511.
- 37 Z. Pajaok, P. Czarnecki, J. Wąsicki and W. Nawrocik, *J. Chem. Phys.*, 1998, **109**, 6420–6423.
- 38 A. Katrusiak and M. Szafranski, *Phys. Rev. Lett.*, 1999, **82**, 576–579.
- 39 X. M. Ren, Q. J. Meng, Y. Song, C. S. Lu, C. J. Hu and X. Y. Chen, *Inorg. Chem.*, 2002, **41**, 5686–5692.
- 40 X. M. Ren, Q. J. Meng, Y. Song, C. J. Hu, C. S. Lu, X. Y. Chen and Z. Xue, *Inorg. Chem.*, 2002, **41**, 5931–5933.
- 41 S. Q. Zang, X. M. Ren, Y. Su, Y. Song, W. J. Tong, Z. P. Ni, H. H. Zhao, S. Gao and Q. J. Meng, *Inorg. Chem.*, 2009, **48**, 9623–9630.
- 42 B. Cai, J. L. Liu, X. L. Sheng and X. M. Ren, *Inorg. Chem. Commun.*, 2011, **14**, 1971–1974.
- 43 R. D. Willett, C. J. Gómez-García, B. L. Ramakrishna and B. Twamley, *Polyhedron*, 2005, **24**, 2232–2237.
- 44 T. Akutagawa, T. Motokizawa, K. Matsuura, S. Nishihara, S. Noro and T. Nakamura, *J. Phys. Chem. B*, 2006, **110**, 5897–5900.
- 45 H. B. Duan, X. R. Chen, H. Yang, X. M. Ren, F. Xuan and S. M. Zhou, *Inorg. Chem.*, 2013, **52**, 3870–3877.
- 46 O. Jeannin, R. Clérac and M. Fourmigué, *J. Am. Chem. Soc.*, 2006, **128**, 14649–14656.
- 47 T. Akutagawa, K. Shitagami, S. Nishihara, S. Takeda, T. Hasegawa, T. Nakamura, Y. Hosokoshi, K. Inoue, S. Ikeuchi, Y. Miyazaki and K. Saito, *J. Am. Chem. Soc.*, 2005, **127**, 4397–4402.
- 48 A. Davison and H. R. Holm, *Inorg. Synth.*, 1967, **10**, 8–26.
- 49 *Software packages SMART and SAINT*, Siemens Analytical X-ray Instrument Inc., Madison, WI, 1996.
- 50 G. M. Sheldrick, *SHELX-97, Program for the refinement of crystal structure*, University of Göttingen, Germany, 1997.
- 51 J. H. van Vleck, *The Theory of Electric and Magnetic Susceptibilities*, Oxford, London, 1932.
- 52 M.-H. Whangbo, H.-J. Koo and D. Dai, *J. Solid State Chem.*, 2003, **176**, 417–481.